Fracture Mechanics of 2D Crystal Blisters with Irregular Geometry

Jiacong Cao, Zhaohe Dai, Chuanli Yu, Wenxiang Wang, Xiaoding Wei, and Yueguang Wei**

Attaching a thin elastic film onto a substrate often traps liquids or gases at the film-substrate interface, resulting in blisters. While typically undesirable, blisters that spontaneously form during the assembly of atomically thin 2D crystals have demonstrated intriguing functionalities—such as high-pressure chemistry and liquid-cell electron microscopy—that exploit the nanoscale confinement of the blister. However, a quantitative understanding of this confinement, including the confining pressure and membrane tension, has been hindered by the irregular shapes of 2D crystal blisters, which occur particularly often in single- or few-layer 2D crystal systems. Here, experiments and theory are combined to reveal how the competition between elastic and adhesive forces in 2D crystal blisters selects the blister shape. It is shown that the geometry of the blister encodes a wealth of useful information, which can be decoded using fracture mechanics concepts, including strain/stress fields, pressure levels, and interface toughness between the 2D crystal and its substrate. These findings have immediate implications for the fabrication and design of 2D crystal-based devices and applications, where blister formation can be either a hindrance or a beneficial feature.

1. Introduction

While two flexible solids with perfectly matching surface geometries can theoretically contact to form a seamless interface, achieving this ideal is usually impractical.[1,2] For example, when applying stickers or facial masks even to flat surfaces, annoying wrinkles or blisters can readily develop,[3] particularly when compressive stresses are inadvertently introduced during the contact process (**Figure** 1A,B).[4–7] Although this issue might be a minor inconvenience in applications such as the placement of stickers,[6,8] it poses significant challenges in the fabrication of electronics.[9] In particular, the device assembly relies heavily on transfer printing of ultra-thin functional films,[10,11] where the formed interfacial blisters can severely compromise device integrity and performance (Figure 1C).[12] The problem is further exacerbated for devices based on atomically thin 2D crystals (Figure 1D),[9,11] as preventing the spontaneous formation of blisters in such systems has been extremely difficult.[13]

Recently, the particular ubiquity of blisters in 2D crystal devices has spurred significant advances not only in a number of nanoscale techniques for their removal,[15–17] but also in a host of fascinating physics and applications that exploit the unique blister confinement.[18–21] For instance, the elastic strain in spontaneous graphene blisters has been found to induce pseudo–magnetic fields greater than 300 Tesla.[22,23] The pressure inside 2D crystal blisters can reach up to 7 GPa, enabling the propagation of solvent-free organic reactions that typically do not occur under standard conditions.[24,25] More recently, the liquid confined within 2D crystal blisters has exhibited diffusion dynamics slowed by a factor of 10^8, enabling liquid-cell electron microscopy as a “slow-motion” camera capable of revealing the conformational substates of biomacromolecules such as DNA.[26–28] Yet, a fundamental question that arises—whether one aims to exploit or eliminate these blisters—is: How do blisters form, and what controls the confinement, such as pressure? This question is typically addressed by focusing on circular 2D crystal blisters,[21,29–33] drawing an analogy to the sessile droplet problem (Figure 1E,F).[34,35] However, unlike droplets with uniform surface tension, 2D crystal blisters generally experience non-uniform elastic membrane tension.[36,37] Consequently, as the crystal thickness decreases, particularly in single-layer systems, the stress states become increasingly complex, and non-circular or irregular blister shapes become more prevalent (as shown in Figure 1D).[14,37,38] Such irregularly shaped blisters have been widely observed but remain poorly understood, directly limiting their applications such as strain engineering and liquid-cell electron microscopy that rely on single-layer 2D crystals often taking irregular blister geometries.[27,28] Here, we address this gap by presenting experiments and a theoretical analysis of the mechanics of irregular 2D crystal blisters. We show that the often observed irregular shape results from a complex interplay of residual, elastic, and adhesive forces. Furthermore, we show that a quantitative understanding of this interplay can reveal a wealth of useful information

J. Cao, Z. Dai, C. Yu, W. Wang, X. Wei, Y. Wei
School of Mechanics and Engineering Science
State Key Laboratory for Turbulence and Complex Systems
Peking University
Beijing 100871, China
E-mail: daizh@pku.edu.cn; weiyg@pku.edu.cn

The ORCID identification number(s) for the author(s) of this article can be found under https://doi.org/10.1002/adfm.202509438

DOI: 10.1002/adfm.202509438

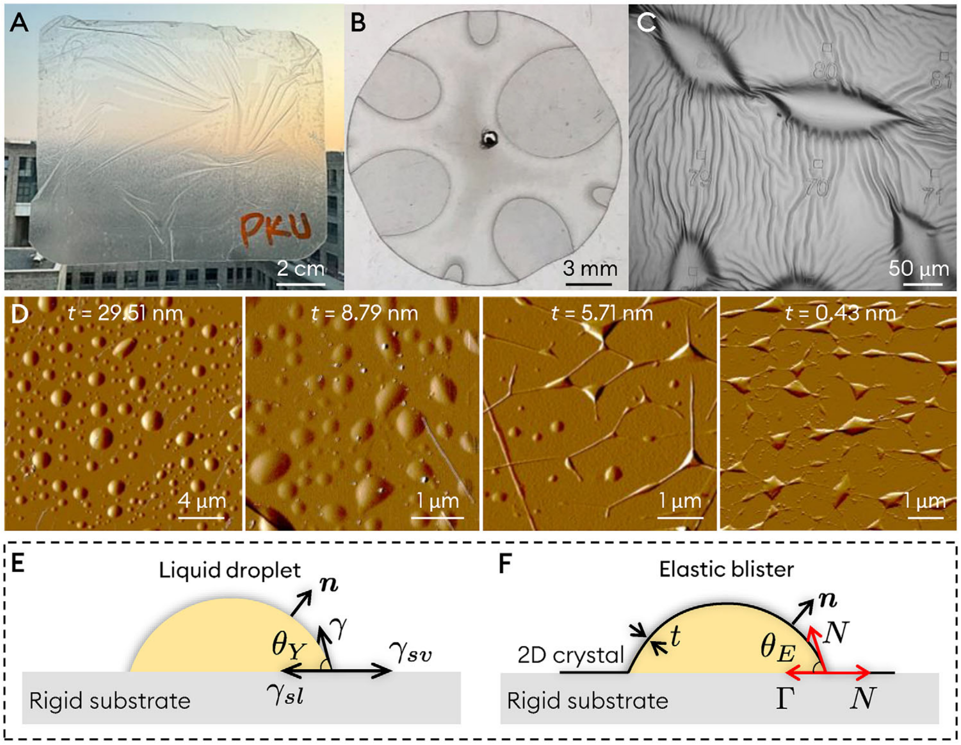

Figure 1. Elastic blisters across multiple scales. A) Photo of a sticker "carelessly" placed on window glass. B) Photo of a thin polymeric sheet partially conforming to a sphere with capillary adhesion. Reproduced with permission.[6] C) Optical image of interfacial blisters formed after the deposition of a 60-nm-thick gold film on a thin PMMA layer. D) AFM amplitude images of blisters formed by transferring graphene sheets onto hBN substrates with water molecules trapped at the interface. Reproduced with permission.[14] E) Schematic illustration of the classical droplet problem, featuring Young's contact angle. F) Schematic illustration of the elastic blister problem, where the liquid is covered by an elastic sheet of Young's modulus E and thickness t, resulting in an elastic version of contact angle.

encoded in the blister geometry, including not only strain, stress, and pressure fields but also the affinity between the crystal and its substrate.

2. Results

We fabricate spontaneously formed graphene blisters on hexagonal Boron Nitride (hBN) and graphite substrate using a wetting transfer method, and characterize their geometry via atomic force microscopy (AFM) (see details in Section S1 Supporting Information).[39] Locally, the blister shape can be described by its principal curvatures, as illustrated in **Figure 2A**. Similar to a typical fracture mechanics problem, understanding blister formation requires solving the boundary value problem for blisters of arbitrary curvature under boundary conditions that are not immediately clear, while also clarifying the appropriate energetic balances in the system. We address these challenges sequentially.

2.1. The Compatibility Equation

In typical few-layer 2D crystal blisters, the deflection is moderate,[30,36] allowing the use of Föppl–von Kármán (FvK) plate theory to describe the deformation of the 2D crystal.[40–42] Since the out-of-plane deformation of the 2D crystal can be directly measured, we focus on the compatibility equation in FvK theory:

$$\frac{1}{Et}\nabla^2\nabla^2\chi(x,y) + K(x,y) = 0 \tag{1}$$

where $\nabla^2 = \partial^2/\partial x^2 + \partial^2/\partial y^2$, E and t denote Young's modulus and the thickness of the 2D crystal, respectively, χ is the Airy stress function to be determined, and K is the local Gaussian curvature of the blister, defined by

$$K = \frac{\partial^2 w}{\partial x^2}\frac{\partial^2 w}{\partial y^2} - \left(\frac{\partial^2 w}{\partial x \partial y}\right)^2 \tag{2}$$

with $w(x, y)$ representing the measured out-of-plane deformation of the 2D crystal (Figure 2A).

We will solve this problem numerically using a spectral method due to its computational efficiency.[43] We follow the approach reported by Darlington et al.,[44] while carefully considering the effect of far-field residual stress $\boldsymbol{T}$ (see Figure 2A). The method transforms the biharmonic equation with a source function Equation (1) into two coupled Poisson equations: $\nabla^2\chi = \Phi(x,y)$ and $\nabla^2\Phi = -EtK(x,y)$. In this context, the boundary conditions arising from the residual stress $\boldsymbol{T}$ are approximated by $\Phi = T_{xx} + T_{yy}$ and $\chi = \frac{1}{2}T_{xx}y^2 + \frac{1}{2}T_{yy}x^2 - T_{xy}xy$ (see Section S2B,

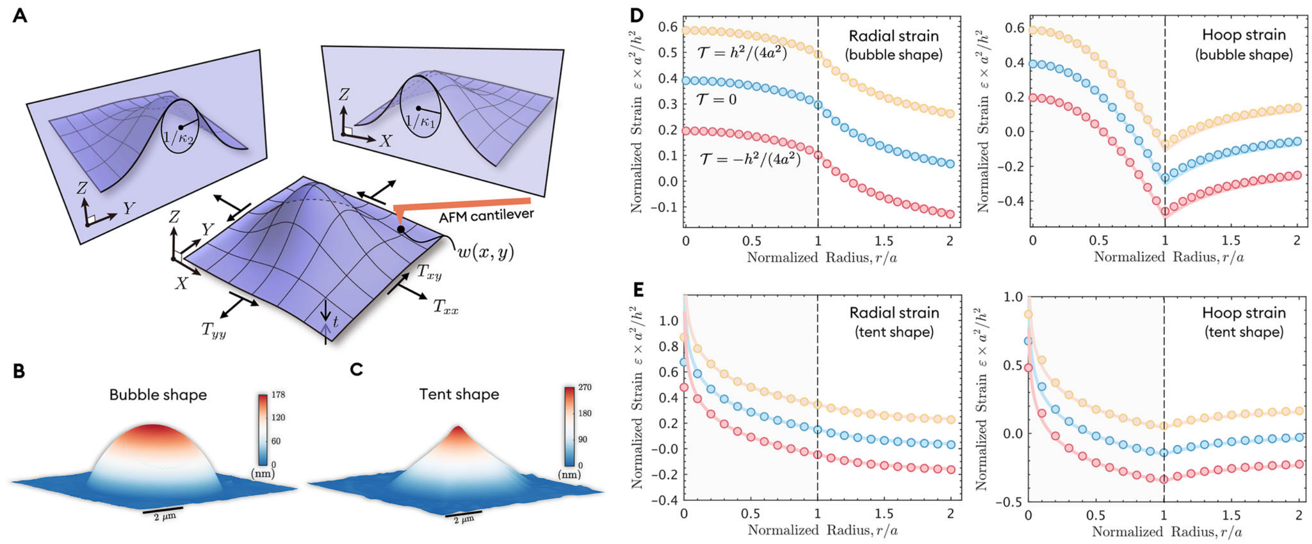

Figure 2. Strain fields in irregular 2D crystal blisters. A) Schematic of a blister subject to a far-field stress field $\boldsymbol{T}$. Its shape is directly measured using AFM, and the local geometry is characterized by the principal curvatures κ_1 and κ_2 (Gaussian curvature $K = \kappa_1 \kappa_2$). B, C) AFM height image of a bubble-like and tent-like multilayer graphene blister. D, E) The radial (left) and hoop (right) strain fields for a circular bubble-like blister (D) and tent-like blister (E) of height h and radius a, subjected to different levels of residual stress. Markers represent numerical calculations (calculated based on $h/a = 0.1$), while solid curves are analytical predictions (given in Section S2.5, Supporting Information).

Supporting Information). We employ a Chebyshev spectral method,[43] which reduces the coupled partial differential equations to two algebraic equations that can be readily solved under the imposed boundary conditions. Details of the numerical scheme are provided in Section S2C (Supporting Information). The stress distribution within the blister is then determined by the calculated Airy stress function χ:

$$N_{xx} = \frac{\partial^2 \chi}{\partial y^2}, \quad N_{yy} = \frac{\partial^2 \chi}{\partial x^2}, \quad \text{and} \quad N_{xy} = -\frac{\partial^2 \chi}{\partial x \partial y} \tag{3}$$

which further yields the strain distribution via Hooke's law and the pressure distribution via FvK equations (Section S2.4, Supporting Information).

Before discussing irregular blisters, we validate our numerical method by calculating the strain distribution for simple, circular blisters—specifically, bubble-like and tent-like blisters commonly observed in experiments, as shown in Figure 2B,C, respectively.[45] For simplicity, we assume that the shape of a single blister is given by

$$w(\boldsymbol{r}) = h\left[1 - \left(\frac{|\boldsymbol{r}|}{a}\right)^{\alpha}\right]\mathcal{H}(a - |\boldsymbol{r}|) \tag{4}$$

where h and a denote the blister height and radius, respectively, $\boldsymbol{r} = (x, y)$ is the polor coordinate, $\mathcal{H}$ is the Heaviside step function. We set $\alpha = 1$ for tent-like blisters and $\alpha = 2$ for bubble-like blisters. Under an equibiaxial residual stress T at infinity, the problem becomes axisymmetric and can be solved analytically (see Section S2.5, Supporting Information). Our numerical calculations are performed using Equation (4) within a square domain of side length $4a$. In Figure 2D,E, we compare the numerically calculated radial and hoop strain distributions (markers) with the analytical solutions (solid curves) under various levels of residual stress. Excellent agreement is observed even near the tent center, where the strain diverges logarithmically. We then proceed to analyze irregular blisters subjected to anisotropic residual stresses, which are typically not well defined a priori.

2.2. Residual Stresses

Direct measurement of residual stresses in thin films has long been challenging.[46] For atomically thin 2D crystals, even advanced techniques such as Raman spectroscopy can yield data that is affected by substrate doping effects.[47] Consequently, previous studies on circular 2D crystal blisters have assumed zero residual stress, which is not well justified.[30,36,37] We will demonstrate that this simplification can lead to an underestimation of both the stress field and the adhesive forces required for equilibrium.

Fortunately, the geometry of irregular blisters itself offers a solution. These blisters (such as the commonly observed triangular blisters) typically exhibit buckled channels at their vertices (**Figure** 3A), which are clear signatures of compressive residual stresses [38,48]. Moreover, the formation of buckles can substantially relieve the compression in ultrathin films, making the assumption of zero residual stress more appropriate.[1,37,48] However, to achieve greater accuracy, we estimate the residual compressive stress, $-T_\infty$, acting perpendicular to the buckled channel based on its geometry. Locally, this reduces to a 1D buckle delamination problem (see Figure 3B), for which the Föppl–von Kármán theory simplifies to $B\frac{d^4w}{dx^4} + T_\infty \frac{d^2w}{dx^2} = 0$, where B is the bending stiffness of the crystal.[49] The solution to the buckling profile is $w = A(1 + \cos 2\pi x/\lambda)$, where A and λ represent the amplitude and wavelength (Figure 3B).[50] As such, the residual stress is given

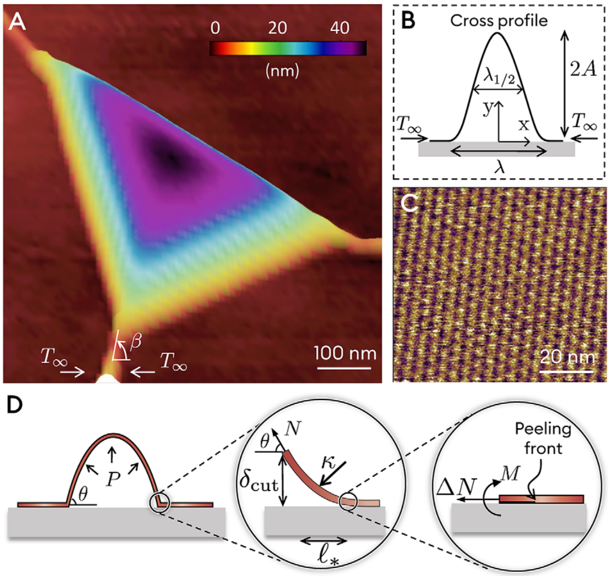

Figure 3. The mechanics of irregular 2D crystal blisters. A) AFM amplitude images of a single triangular blister formed by transferring a monolayer graphene sheet onto a boron nitride substrate, featuring three small buckles at the vertices. B) Schematic cross-section of the buckle, characterized by its amplitude A and wavelength λ. C) The moiré pattern formed between the graphene sheet and the boron nitride substrate in the blister-free region, indicating that the interface is atomically smooth and clean. D) Schematic illustration of the delamination at the blister edge. At the scale of the blister radius, an apparent contact angle is observed, whereas at the scale of $\ell_* \sim (B/N)^{1/2}$, the film makes contact with the substrate smoothly.

by the critical Euler buckling force,[46,50,51] which relates to the buckle geometry via

$$T_\infty(\beta) = \pi^2 B/\lambda_{1/2}^2 \tag{5}$$

where β is the in-plane orientation angle of the buckle and $\lambda_{1/2}$ is the half-peak width of the buckle cross profile, as illustrated in Figure 3B. We adopt $\lambda_{1/2}$ because it is more readily assessable than the full wavelength in experiments.

We can then apply this approach to all three buckles that form a "rosette strain gauge", allowing for the estimation of the three residual stress components. We find that $T_\infty/Et \lesssim 10^{-5} \ll 1$ in the triangular few-layer graphene blisters observed in our experiments. As a consequence, the numerical results suggest that it is fairly legitimate to assume zero residual stress when calculating the strain and stress fields in buckled irregular blisters (note that this would not be the case for round blisters that may experience some unknown, non-negligible residual tension). Notably, the simple form of Equation (5) benefits from the lubricated interface between the 2D crystal and its hBN substrate, thereby avoiding complex mode-mixity.[52,53] This lubrication essentially arises from the incommensurate contact at the interface, as evidenced by the formation of moiré patterns in regions outside the graphene-on-hBN blister (Figure 3C).[54–56]

2.3. The Energy Release Rate

Having completed the boundary value problem, we now turn to the elastoadhesive interaction in irregular blisters. Since blister formation is a spontaneous process, we expect a local force balance at the blister edge, i.e.,

$$\mathcal{G} = \Gamma \tag{6}$$

where $\mathcal{G}$ is the energy release rate that drives the peeling of the 2D crystal from its substrate, and Γ is the interface toughness or adhesion energy that resists delamination or promotes interface closure.[46] This balance implies that our method measures the apparent adhesion energy. Note that there are possible electrostatic interactions due to the charge doping effects in these vdW heterostructures, though typically negligible compared to the dominant elastoadhesive forces.[57]

Thanks to the relatively straight blister edges observed in irregular blisters (Figure 3A), we can invoke the 1D thin film delamination problem,[46,52] for which the energy release rate is given by

$$\mathcal{G} = \frac{M^2}{2B} + \frac{\Delta N^2}{2E't} \tag{7}$$

where M denotes the torque exerted by the film at the crack front, E' is the plane-strain Young's modulus of the crystal, and ΔN represents the difference in membrane tension across the crack front, as illustrated in Figure 3D. A boundary layer analysis presented in Section S3.1 (Supporting Information) indicates that evaluating Equation (7) requires sophisticated measurements of the blister curvature within a region of size $\ell_* = \sqrt{B/N}$ near the crack front, where N is membrane tension at the blister edge (see Figure 3D). For typical few-layer 2D crystal blisters, where $B \lesssim 100\,\text{nN}\cdot\text{nm}$ and $N \sim E't/100$, we estimate that $\ell_* \lesssim 4$ nm, which greatly limits the direct application of Equation (7).

By contrast, when observing at the scale of the blister radius (Figure 3D),[58] we can utilize a well-defined contact angle θ and a numerically calculable membrane stress state near the blister edge. Inspired by Kendall's peeling theory,[59] the energy release rate is given by

$$\mathcal{G} = N(1 - \cos\theta) \tag{8}$$

As such, the equilibrium condition $G = \gamma$ implies an elastic analog of Young's contact angle at the blister edge (see the comparison between Figure 1E,F). It can be shown that the two methods for evaluating the energy release rate are, in fact, identical (Section 3, Supporting Information), as long as the contact angle is consistently revealed by cutting the blister at a height $\delta_{cut} \gg \ell_*\theta$, i.e.,

$$\delta_{cut} \gg \theta\sqrt{B/N} \quad \text{and} \quad N > 0 \tag{9}$$

which can be readily achieved in practice. We note that the cut-off height cannot be arbitrarily large as the observed contact angle decreases with increasing δ_{cut}. To avoid significant deviations, we set δ_{cut} to be one-tenth of the maximum blister height while satisfying Equation (9) and $\delta_{cut} < \theta^2 P/(30N)$, where P is the maximum pressure of the blister (based on a scaling analysis in Section 3.2,

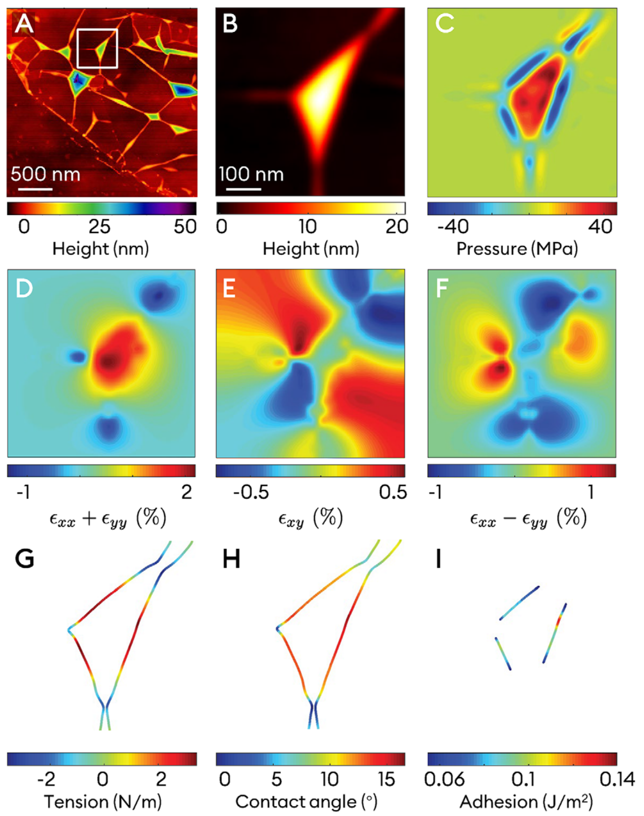

Figure 4. Revealing the elastoadhesive interaction in irregular 2D crystal blisters. AFM height image of monolayer graphene on a graphite substrate containing many blisters (A) and an intercepted single blister (B). C) Pressure distribution calculated from the height profile of the blister in (B). D,F) Computed strain distributions based on (C). G, H) The normal membrane tension and contact angle along the edge of the blister, defined by the cut-off height δ_{cut}. I) Adhesion energy calculated via Equation (8), satisfying the criterion in Equation (9). Note that the scale bar in (C-I) is identical to that in (B).

Supporting Information). By considering perfectly circular blisters of shape given by Equation (4) (for which $\mathcal{G}$ can be provided analytically), we test the energy release rate obtained this way, producing relative errors within 10% (see Figures S4, Supporting Information).

3. Discussion

Finally, we apply the fracture mechanics framework outlined in the preceding section to gain a quantitative understanding of the elastoadhesive interactions in irregular 2D crystal blisters that have been frequently observed in many single-layer 2D crystal-based applications.[19,27,28,30,36]

3.1. Strain, Tension, and Adhesion

Figure 4A shows a typical AFM height image of a monolayer graphene sheet transferred onto a graphite substrate via wetting transfer. Numerous triangular and polygonal blisters with relatively straight edges are observed. To demonstrate the analysis process, we select a triangular blister (highlighted by the white box in Figure 4A) and reproduce it in Figure 4B. We apply Gaussian smoothing to eliminate noise from the experimental data. The resulting blister height profile is then used to compute the Gaussian curvature function, which is substituted into Equation (1) to formulate the problem. The boundary residual stresses are estimated from the morphology of the three buckles at the blister vertices, according to Equation (5) and the associated stress transformation. We then employ the numerical scheme discussed in the preceding section to solve for the Airy stress function. Finally, the pressure and strain fields are obtained using Equation (3) and Hooke's law (see the results for the selected blister in Figures 4C–F). In Figure S2 (Supporting Information), we also show similar results for monolayer and four-layer graphene blisters on hBN substrates.

Figure 4D indicates that the strain within the blister is predominantly tensile, with a magnitude of approximately 1%. This observation is consistent with a rough estimation based on the blister geometry, in which the strain is expected to scale as h^2/a^2—here, $h \approx 10$ nm represents the typical blister height and $a \approx 100$ nm the typical blister size (see Figure 4B). In contrast, the buckled regions exhibit compressive strains; however, these quantitative values may be less reliable due to the insufficient resolution of the height data for the small buckles. Moreover, the pressure within the blister-confined region is relatively uniform, with a value on the order of 10 MPa (Figure 4C). This is consistent with a rough estimation of Eth^3/a^4 derived from the analysis of circular blisters.[60] Intriguingly, a negative pressure region appears near the blister edge in Figure 4C. This phenomenon can be attributed to the strong short-range attractive forces, such as van der Waals interactions between the 2D crystal and the substrate.

In Figure 4G–H, we make a horizontal cut through the blister to expose its edge along with the normal membrane tension acting perpendicular to it, the local contact angle, and—by applying the equilibrium condition Equation (6) and the energy release rate Equation (8)—the corresponding interface toughness. On the straight blister edges, the membrane tension is mostly positive, effectively playing a role analogous to a peeling force with a peeling angle θ. Moreover, the blister rotation is relatively modest (with $\theta^2 \lesssim 0.07$), which justifies the use of Föppl–von Kármán theory. We can then calculate the interface toughness (i.e., the adhesion between the graphene sheet and the graphite substrate) based on Equation (8), which lies between 80 and 120 mJ m^{-2} in this sample, in good agreement with previously reported indirect measurements (86–221 mJ m^{-2})[36,61] (A comparison with the literature is provided in Table S1, Supporting Information).

3.2. Apparent Interface Toughness

We then apply our framework to triangular blisters observed across three material systems: monolayer graphene on graphite, monolayer graphene on hBN, and four-layer graphene on hBN. The membrane tension and contact angle measured at the blister edges (which satisfy the scaling requirement given in Equation (9)) are summarized in **Figure** 5A, with approximately 100 data points plotted for each straight blister edge (involving around 10–20 edges for each group). The local $N \propto \theta^{-2}$ relation in Figure 5A agrees with the condition for the balance of

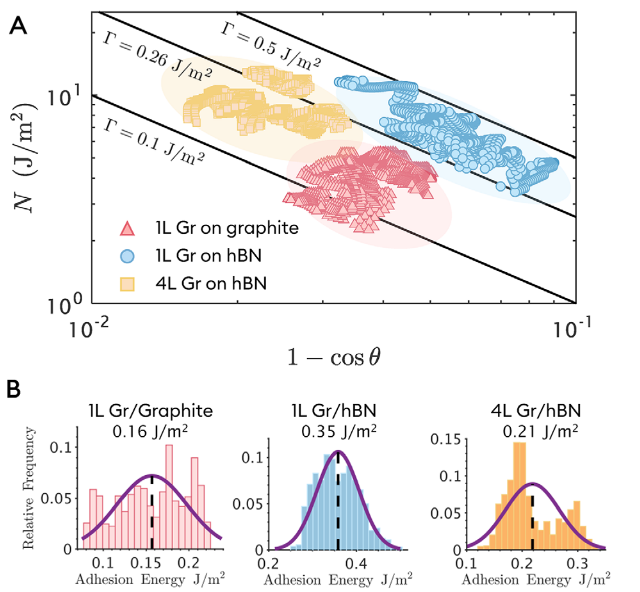

Figure 5. The elastoadhesive interaction at the blister edge. A) Relationship between the membrane tension and local contact angles measured from three different pairs of materials: monolayer graphene on graphite substrate, monolayer graphene on hBN substrate, and four-layer graphene on hBN substrate. The solid lines are based on Equations (6) and (8) with different adhesion energies. B) The extracted adhesion energy for the three pairs of interface.

elastic and adhesive forces in Equation (8). The resulting apparent adhesion is then calculated. We find that the distribution of adhesion values calculated from the same blister is relatively concentrated, whereas calculations from different blisters tend to be dispersed. We attribute the dispersion to mixed mode fracture at the blister edge.[52] While the mechanics at the actual interfaces are complicated by coupled normal (adhesion) and tangential (friction/shear) interactions,[53] our model focuses on the mode I fracture. This simplification likely accounts for the observed variation in adhesion energy across different blisters on the same substrate. Despite this dispersion, the overall values are stable, as presented in Figure 5B for three interfaces: monolayer graphene on graphite (0.06–0.23 J m^{-2}), monolayer graphene on hBN (0.26–0.5 J m^{-2}), and four-layer graphene on hBN (0.11–0.32 J m^{-2}). Notably, the results indicate that the graphene–hBN affinity is systematically stronger than the graphene–graphite affinity, which aligns with practical experiments demonstrating that hBN is an effective stamp for picking up graphene sheets from various substrates, including graphite.[9,11,62] In addition, the apparent adhesion is found to decrease with the thickness of the graphene sheets, likely due to the reduced conformal contact for relatively thick crystals, which agrees with previous experiments and simulations.[53,63,64]

The framework discussed can, of course, be applied to relatively round blisters. However, as mentioned before, it is unclear what the residual stress is in this case. A natural option is to assume vanishing far-field stress, as in previous analytical models.[30,32,36,45,65] With this assumption, we use our framework to calculate the apparent adhesion based on circular blisters in Figure S5 (Supporting Information), which agrees well with predictions from analytical models,[30,32,36,45,65] even though circular blisters could undergo complex wrinkling patterns near the contact line.[37,60] Nonetheless, the adhesion energy estimated from circular blisters is found to be significantly lower than that from triangular blisters (Figure S5, Supporting Information). This discrepancy might be attributed to non-trivial far-field stresses in circular blisters that we have had to neglect. Therefore, caution is needed when using round blisters for adhesion estimation due to the unclear far-field stress state, highlighting the need for further investigation. By contrast, the residual stresses are largely released in triangular blisters through edge buckles, providing a better platform for characterizing the strain fields and energy release rate. This may explain why the adhesion energies estimated via circular spontaneous 2D crystals have been systematically lower than those measured via other methods, such as the double cantilever beam test.[53]

4. Conclusion

In conclusion, we have developed a fracture mechanics framework to quantitatively understand the interplay of adhesive and elastic forces in irregular, spontaneously formed 2D crystal blisters. Our approach enables a more accurate measurement of the blister strain distribution by using strain gauges to estimate the far-field stress state. Looking forward, our method can be integrated with data-driven techniques like machine learning to enable rapid strain sensing in the nanoscale. We have shown that a quantitative understanding of such elastoadhesive interactions can reveal a number of useful information, including the strain and stress fields and internal pressure in blisters, which have been elusive previously. Interestingly, though exhibiting diverse shapes, blisters show local membrane tensions that are approximately inversely proportional to the square of the local contact angle due to the elastoadhesive interactions. Although we use water-filled blisters here, our theoretical framework is based on continuum mechanics (FvK plate theory and fracture mechanics) and does not make any assumptions about the substance trapped inside the blister, other than that it exerts a pressure on the film. Therefore, the model is, in principle, applicable to gas-filled blisters. Moreover, the fracture mechanics framework presented here is not limited to graphene and can be generalized to other 2D materials and flexible thin films, achieving high-throughput adhesion energy analysis in the future. Overall, our results have direct applications in strain engineering, adhesion mechanics, high-pressure chemistry, and liquid-cell electron microscopy, where few-layer 2D crystals often take irregular blister shapes and understanding the mechanics of nanoscale confinement is crucial.

5. Experimental Section

Spontaneous water blisters were prepared by employing a water-assisted wetting transfer method to deposit 2D crystals onto an hBN substrate in ambient air.[39] AFM phase and height images were acquired using an Asylum Research Cypher.[17] The inhomogeneous biharmonic equation was solved via a Chebyshev spectral method.[43] In this approach, the objective function was first expanded in finite-order Chebyshev polynomials of the first kind, which were interpolated at Gauss-Chebyshev-Lobatto points ($x_j = \cos j\pi/N$, $\sim j = 0, 1, \ldots, N$). The interpolating polynomials were then differentiated at these Chebyshev points to approximate the derivatives of the objective function. This linear procedure converted the differentiation operation into a matrix operation, yielding the so-called Chebyshev spectral differentiation matrix. Finally, the partial differential equations were transformed into algebraic equations by applying this derivation matrix together with the far-field stress boundary conditions. Extended experimental results and additional details on the theoretical models and numerical scheme could be found in the Supporting Information.

Supporting Information

Supporting Information is available from the Wiley Online Library or from the author.

Acknowledgements

This work was supported by the National Natural Science Foundation of China (Grant Nos. 12372103 and 12432003). The authors thank Huan Wang for the discussion of liquid cell microscopy.

Conflict of Interest

The authors declare no conflict of interest.

Data Availability Statement

The data that support the findings of this study are available from the corresponding author upon reasonable request.

Keywords

2D crystals, delamination, energy release rate, thin films

Received: April 15, 2025
Revised: June 26, 2025
Published online:

[1] D. Vella, *Nat. Rev. Phys.* **2019**, *1*, 425.
[2] A. Juel, D. Pihler-Puzović, M. Heil, *Annu. Rev. Fluid Mech.* **2018**, *50*, 691.
[3] Y. Aoyanagi, J. Hure, J. Bico, B. Roman, *Soft Matter* **2010**, *6*, 5720.
[4] J. Hure, B. Roman, J. Bico, *Phys. Rev. Lett.* **2011**, *106*, 174301.
[5] F. Box, L. Domino, T. O. Corvo, M. Adda-Bedia, V. Démery, D. Vella, B. Davidovitch, *Proc. Natl. Acad. Sci. USA* **2023**, *120*, 2212290120.
[6] S. Liu, J. He, Y. Rao, Z. Dai, H. Ye, J. C. Tanir, Y. Li, N. Lu, *Sci. Adv.* **2023**, *9*, eadf2709.
[7] J. Chopin, D. Vella, A. Boudaoud, *Proc. R. Soc. A: Math., Phys. Eng. Sci.* **2008**, *464*, 2887.
[8] C. Choi, M. K. Choi, S. Liu, M. Kim, O. K. Park, C. Im, J. Kim, X. Qin, G. J. Lee, K. W. Cho, M. Kim, E. Joh, J. Lee, D. Son, S. Kwon, N. L. Jeon, Y. M. Song, N. Lu, D. Kim, *Nat. Commun.* **2017**, *8*, 1664.
[9] K. S. Novoselov, A. Mishchenko, A. Carvalho, A. Castro Neto, *Science* **2016**, *353*, aac9439.
[10] J. A. Rogers, T. Someya, Y. Huang, *Science* **2010**, *327*, 1603.
[11] A. Castellanos-Gomez, X. Duan, Z. Fei, H. R. Gutierrez, Y. Huang, X. Huang, J. Quereda, Q. Qian, E. Sutter, P. Sutter, *Nat. Rev. Methods Primers* **2022**, *2*, 58.
[12] A. V. Kretinin, Y. Cao, J.-S. Tu, G. Yu, R. Jalil, K. S. Novoselov, S. J. Haigh, A. Gholinia, A. Mishchenko, M. Lozada, T. Georgiou, C. R. Woods, F. Withers, P. Blake, G. Eda, A. Wirsig, C. Hucho, K. Watanabe, T. Taniguchi, A. K. Geim, R. V. Gorbachev, *Nano Lett.* **2014**, *14*, 3270.
[13] D. A. Sanchez, Z. Dai, N. Lu, *Trends Chem.* **2021**, *3*, 204.
[14] W. Wang, X. Ma, Z. Dai, S. Zhang, Y. Hou, G. Wang, Q. Li, Z. Zhang, Y. Wei, L. Liu, *Adv. Mater. Interfaces* **2022**, *9*, 2101939.
[15] F. Pizzocchero, L. Gammelgaard, B. S. Jessen, J. M. Caridad, L. Wang, J. Hone, P. Bøggild, T. J. Booth, *Nat. Commun.* **2016**, *7*, 11894.
[16] W. Dong, Z. Dai, L. Liu, Z. Zhang, *Adv. Mater.* **2024**, *36*, 2303014.
[17] Y. Hou, Z. Dai, S. Zhang, S. Feng, G. Wang, L. Liu, Z. Xu, Q. Li, Z. Zhang, *Nat. Commun.* **2021**, *12*, 5069.
[18] Z. Dai, L. Liu, Z. Zhang, *Adv. Mater.* **2019**, *31*, 1805417.
[19] P. Ares, T. Cea, M. Holwill, Y. B. Wang, R. Roldán, F. Guinea, D. V. Andreeva, L. Fumagalli, K. S. Novoselov, C. R. Woods, *Adv. Mater.* **2020**, *32*, 1905504.
[20] E. Stellino, B. D'Alò, E. Blundo, P. Postorino, A. Polimeni, *Nano Lett.* **2024**, *24*, 3945.
[21] B. Li, W. Tan, C. Shen, Y. Long, Z. Gao, J. Wang, W. Guo, J. Yin, *J. Mech. Phys. Solids* **2024**, *190*, 105723.
[22] N. Levy, S. Burke, K. Meaker, M. Panlasigui, A. Zettl, F. Guinea, A. C. Neto, M. F. Crommie, *Science* **2010**, *329*, 544.
[23] D.-H. Kang, H. Sun, M. Luo, K. Lu, M. Chen, Y. Kim, Y. Jung, X. Gao, S. J. Parluhutan, J. Ge, S. W. Koh, D. Giovanni, T. C. Sum, Q. J. Wang, H. Li, D. Nam, *Nat. Commun.* **2021**, *12*, 5087.
[24] C. H. Y. X. Lim, M. Nesladek, K. P. Loh, *Angew. Chem., Int. Ed.* **2014**, *53*, 215.
[25] S. In Yoon, H. Park, Y. Lee, C. Guo, Y. J. Kim, J. S. Lee, S. Son, M. Choe, D. Han, K. Kwon, J. Lee, K. Y. Ma, A. Ghassami, S. W. Moon, S. Park, B. K. Kang, Y. Kim, S. Koo, A. Genco, A. Tartakovskii, Y. Duan, F. Ding, S. Ahn, S. Ryu, J. Kim, W. S. Yang, M. Chhowalla, Y. S. Park, S. K. Min, Z. Lee, et al., *Sci. Adv.* **2024**, *10*, eadp9804.
[26] S. Kang, J.-H. Kim, M. Lee, J. W. Yu, J. Kim, D. Kang, H. Baek, Y. Bae, B. H. Kim, S. Kang, S. Shim, S. Park, W. B. Lee, T. Hyeon, J. Sung, J. Park, *Sci. Adv.* **2021**, *7*, eabi5419.
[27] A. Pedrazo-Tardajos, N. Claes, D. Wang, A. Sánchez-Iglesias, P. Nandi, K. Jenkinson, R. De Meyer, L. M. Liz-Marzán, S. Bals, *Nat. Chem.* **2024**, *16*, 1278.
[28] J.-Y. Li, F. Liu, J. Xu, Y.-J. Kim, O.-H. Kwon, B. Xia, H. Wang, S. Granick, *Proc. Natl. Acad. Sci. USA* **2024**, *121*, 2314797121.
[29] K. Yue, W. Gao, R. Huang, K. M. Liechti, *J. Appl. Phys.* **2012**, *112*, 083512.
[30] E. Khestanova, F. Guinea, L. Fumagalli, A. Geim, I. Grigorieva, *Nat. Commun.* **2016**, *7*, 12587.
[31] H. Ghorbanfekr-Kalashami, K. Vasu, R. R. Nair, F. M. Peeters, M. Neek-Amal, *Nat. Commun.* **2017**, *8*, 15844.
[32] E. Blundo, T. Yildirim, G. Pettinari, A. Polimeni, *Phys. Rev. Lett.* **2021**, *127*, 046101.
[33] Z. Dai, *J. Appl. Mech.* **2024**, *91*, 081002.
[34] Y. Rao, S. Qiao, Z. Dai, N. Lu, *J. Mech. Phys. Solids* **2021**, *151*, 104399.
[35] J. Bico, É. Reyssat, B. Roman, *Annu. Rev. Fluid Mech.* **2018**, *50*, 629.
[36] D. A. Sanchez, Z. Dai, P. Wang, A. Cantu-Chavez, C. J. Brennan, R. Huang, N. Lu, *Proc. Natl. Acad. Sci. USA* **2018**, *115*, 7884.
[37] P. Ares, Y. B. Wang, C. R. Woods, J. Dougherty, L. Fumagalli, F. Guinea, B. Davidovitch, K. S. Novoselov, *Proc. Natl. Acad. Sci. USA* **2021**, *118*, 2025870118.
[38] K. Zhang, M. Arroyo, *Extreme Mech. Lett.* **2017**, *14*, 23.
[39] Y. Hou, X. Ren, J. Fan, G. Wang, Z. Dai, C. Jin, W. Wang, Y. Zhu, S. Zhang, L. Liu, Z. Zhang, *ACS Appl. Mater. Interfaces* **2020**, *12*, 40958.
[40] W. Gao, R. Huang, *J. Mech. Phys. Solids* **2014**, *66*, 42.
[41] M. Zelisko, F. Ahmadpoor, H. Gao, P. Sharma, *Phys. Rev. Lett.* **2017**, *119*, 068002.
[42] E. H. Mansfield, *The bending and stretching of plates*, Cambridge University Press, Cambridge, England, **2005**.

[43] L. N. Trefethen, *Spectral methods in MATLAB*, SIAM, **2000**.
[44] T. P. Darlington, A. Krayev, V. Venkatesh, R. Saxena, J. W. Kysar, N. J. Borys, D. Jariwala, P. J. Schuck, *J. Chem. Phys.* **2020**, *153*, 024702.
[45] Z. Dai, Y. Hou, D. A. Sanchez, G. Wang, C. J. Brennan, Z. Zhang, L. Liu, N. Lu, *Phys. Rev. Lett.* **2018**, *121*, 266101.
[46] L. B. Freund, S. Suresh, *Thin film materials: stress, defect formation and surface evolution*, Cambridge university Press, Cambridge **2004**.
[47] A. C. Ferrari, J. C. Meyer, V. Scardaci, C. Casiraghi, M. Lazzeri, F. Mauri, S. Piscanec, D. Jiang, K. S. Novoselov, S. Roth, A. K. Geim, *Phys. Rev. Lett.* **2006**, *97*, 187401.
[48] Z. Dai, D. A. Sanchez, C. J. Brennan, N. Lu, *J. Mech. Phys. Solids* **2020**, *137*, 103843.
[49] G. Wang, Z. Dai, J. Xiao, S. Feng, C. Weng, L. Liu, Z. Xu, R. Huang, Z. Zhang, *Phys. Rev. Lett.* **2019**, *123*, 116101.
[50] D. Vella, J. Bico, A. Boudaoud, B. Roman, P. M. Reis, *Proc. Natl. Acad. Sci. USA* **2009**, *106*, 10901.
[51] H. Mei, C. M. Landis, R. Huang, *Mech. Mater.* **2011**, *43*, 627.
[52] J. W. Hutchinson, Z. Suo, *Adv. Appl. Mech.* **1991**, *29*, 63.
[53] Z. Dai, N. Lu, K. M. Liechti, R. Huang, *Curr. Opin. Solid State Mater. Sci.* **2020**, *24*, 100837.
[54] G. Wang, Z. Dai, Y. Wang, P. Tan, L. Liu, Z. Xu, Y. Wei, R. Huang, Z. Zhang, *Phys. Rev. Lett.* **2017**, *119*, 036101.
[55] Y. Song, D. Mandelli, O. Hod, M. Urbakh, M. Ma, Q. Zheng, *Nat. Mater.* **2018**, *17*, 894.
[56] O. Hod, E. Meyer, Q. Zheng, M. Urbakh, *Nature* **2018**, *563*, 485.
[57] X. Wang, Z. Kou, R. Qiao, Y. Long, B. Li, X. Li, W. Guo, X. Liu, J. Yin, *Nat. Commun.* **2025**, *16*, 324.
[58] C. Yu, W. Zeng, B. Wang, X. Cui, Z. Gao, J. Yin, L. Liu, X. Wei, Y. Wei, Z. Dai, *Nano Lett.* **2025**, *25*, 1876.
[59] K. Kendall, *J. Phys. D: Appl. Phys.* **1975**, *8*, 1449.
[60] Z. Dai, N. Lu, *J. Mech. Phys. Solids* **2021**, *149*, 104320.
[61] J. Wang, D. C. Sorescu, S. Jeon, A. Belianinov, S. V. Kalinin, A. P. Baddorf, P. Maksymovych, *Nat. Commun.* **2016**, *7*, 13263.
[62] E. Han, J. Yu, E. Annevelink, J. Son, D. A. Kang, K. Watanabe, T. Taniguchi, E. Ertekin, P. Y. Huang, A. M. van der Zande, *Nat. Mater.* **2020**, *19*, 305.
[63] S. P. Koenig, N. G. Boddeti, M. L. Dunn, J. S. Bunch, *Nat. Nanotechnol.* **2011**, *6*, 543.
[64] W. Gao, R. Huang, *J. Phys. D: Appl. Phys.* **2011**, *44*, 452001.
[65] Z. Dai, Y. Rao, N. Lu, *Int. J. Solids Struct.* **2022**, *257*, 111829.